Chemical Geology 259 (2009) 17–29

Contents lists available at ScienceDirect

Chemical Geology

journal homepage: www.elsevier.com/locate/chemgeo

An in situ X-ray absorption spectroscopy study of gold-chloride complexing in hydrothermal fluids

Gleb S. Pokrovski [a,*], Boris R. Tagirov [b], Jacques Schott [a], Elena F. Bazarkina [a,b], Jean-Louis Hazemann [c], Olivier Proux [d]

[a] Experimental Geochemistry and Biogeochemistry Group, Laboratoire des Mécanismes et Transferts en Géologie, LMTG - Université de Toulouse - CNRS - IRD - OMP, 14 Av. E. Belin, F-31400 Toulouse, France
[b] Institute of Ore Deposits Geology, IGEM RAS, Staromonetniy per. 35, 119017 Moscow, Russia
[c] Institut Néel, CNRS, 25 avenue des Martyrs, F-38042 Grenoble Cedex 9, France
[d] Laboratoire de Géophysique Interne et Tectonophysique, UMR CNRS - Université Joseph Fourier, 1381 rue de la Piscine, Domaine Universitaire, F-38400 Saint-Martin-d'Hères, France

ARTICLE INFO

Article history:
Accepted 5 September 2008

Keywords:
Gold
XAFS spectroscopy
Chloride complexes
Quantum-chemical modeling
Hydrothermal fluid

ABSTRACT

Despite the growing body of experimental data on gold solubility in hydrothermal fluids, the identity, structure and stoichiometry of Au-bearing aqueous complexes remain poorly known. Here we present the first in situ measurements, using X-ray absorption fine structure (XAFS) spectroscopy, of the stability and structures of Au^{III} and Au^{I} chloride complexes at elevated temperatures and pressures (*T*–*P*) typical of natural hydrothermal conditions. The $HAuCl_4$–NaCl–HCl–$Au_{(s)}$ and NaCl–H_2SO_4–$Au_{(s)}$ systems were investigated to 500 °C and 600 bar using a recently designed X-ray cell which allows simultaneous determination of the absolute concentration of the absorbing atom (Au) and its local atomic environment in the fluid phase. XAFS data combined with Density Functional Theory quantum-chemical calculations of species structures and ab-initio modeling of XANES spectra show that the $Au^{III}Cl_4^-$ species is rapidly reduced to $Au^{I}Cl_2^-$ at temperatures above 100–150 °C in acidic NaCl–HCl solutions. In the latter complex, two chlorine atoms are aligned in a linear geometry around Au at an average distance of 2.267±0.004 Å. Our data provide the first direct structural evidence for $AuCl_2^-$, which is the major Au-bearing species in acidic Cl-rich hydrothermal fluids over a wide *T*–*P* range, in agreement with previous solubility and Raman spectroscopy data. Total aqueous Au concentrations measured by XAFS in $HAuCl_4$–HCl–NaCl and NaCl–H_2SO_4 solutions in the presence of $Au_{(s)}$ are, however, one to two orders of magnitude lower than those predicted by equilibrium thermodynamic calculations. This discrepancy is believed to be due to the combined effects of the cell properties, X-ray beam induced phenomena, and kinetic factors which may complicate the interpretation of high *T*–*P* spectroscopic data in redox-sensitive systems.

1. Introduction

Knowledge of the identity, stability and structure of gold aqueous complexes is indispensable for understanding the transport, distribution and deposition of this precious metal by ore-forming fluids. As a result, many studies have been devoted, over almost 40 years, to quantifying gold interactions with major natural ligands like hydroxide, chloride and sulfide (see Stefánsson and Seward, 2003a,b; Tagirov et al., 2005, 2006; references therein). Most of these studies have been performed using solubility methods or synthetic fluid inclusion techniques in hydrothermal reactors involving high temperature–pressure (*T*–*P*) fluid sampling or quenching to ambient conditions. However, the "noble" nature of Au resulting in low solubilities and rapid kinetics of reduction of both principal gold forms in solution, monovalent Au^{I} and trivalent Au^{III}, into native metal poses a formidable challenge for experimentalists, and is responsible for the large discrepancies affecting both the stability constants and stoichiometries of Au-bearing aqueous species derived from bulk solubility data. Here we report new structural and stability data for Au^{III} and Au^{I} chloride complexes obtained at elevated temperatures using in situ XAFS spectroscopy, thermodynamic modeling and quantum-chemical calculations.

Auric gold (Au^{III}) chloride complexes are recognized as primary aqueous Au species in oxidizing surficial environments at acidic and neutral conditions, whereas aurous gold (Au^{I}) chloride species form at elevated temperatures in hydrothermal Cl-rich fluids (e.g., Gammons and Williams-Jones, 1997; Akinfiev and Zotov, 2001; Berrodier et al., 2004). The stoichiometry and stability of Au^{III}–Cl complexes have been studied at ambient conditions using potentiometry (Nikolaeva et al., 1972), Raman (Peck et al., 1991; Murphy and LaGrange, 1998), and XAFS (Farges et al., 1993; Berrodier et al., 2004) spectroscopy which show that the square-plane $AuCl_4^-$ dominates in acidic solutions (pH ≤ ~5) and is progressively replaced by mixed $AuCl_n(OH)_{4-n}$ species

* Corresponding author. Tel.: +33 5 61 33 26 18; fax: +33 5 61 33 25 60.
E-mail address: pokrovsk@lmtg.obs-mip.fr (G.S. Pokrovski).

0009-2541/$ – see front matter © 2008 Elsevier B.V. All rights reserved.
doi:10.1016/j.chemgeo.2008.09.007

with increasing solution pH. No data are available, however, on the structure of Au^{III}–Cl species at temperatures above ambient.

The formation conditions and structure of Au^{I} chloride complexes are much less constrained owing to their low stability at ambient *T–P* and weak solubility even at high temperatures. A number of solubility studies have reported the formation constants for the $AuCl_2^-$ species presumed to be dominant in natural acidic chloride-rich fluids at elevated *T–P* (Henley, 1973; Wood et al., 1987; Zotov and Baranova, 1989; Gammons and Williams-Jones, 1995, 1997; Stefánsson and Seward, 2003b). The agreement between studies carried out since the 1990's is rather good with a scatter of $AuCl_2^-$ formation constant values of less than 0.3 log units to 450 °C and 1500 bar (see Stefánsson and Seward, 2003b for discussion). In addition, a few attempts have been undertaken to detect this species by in situ Raman spectroscopy at temperatures up to 300 °C (Pan and Wood, 1991; Murphy et al., 2000), but they led to somewhat contradictory results regarding both Raman band assignments and Au^{I}–Au^{III} transformation conditions in chloride solutions. Thus, direct evidence for the formation of aurous chloride species is still lacking and their stoichiometry and structure remain poorly constrained. Clearly, more in situ studies are needed to better understand and quantify the stabilities and structures of Au species in the system Au^{I}–Au^{III}–Cl at hydrothermal *T–P*.

With the advent of in situ spectroscopic methods and improvement of synchrotron radiation sources in the last 10–15 years, it has become possible to rigorously assess the local atomic structures of metals in high *T–P* aqueous fluids (e.g., see Seward and Driesner, 2004). These in situ data, complemented by quantum-chemical and molecular dynamics calculations (e.g., Sherman, 2001) and ab-initio modeling of X-ray absorption spectra (e.g., see Rehr, 2006 for a recent review), are going to provide unprecedented insights into the identities and structures of metal complexes in hydrothermal fluids. In addition, quite recently, a few in situ spectroscopic studies combining *simultaneous measurement* of mineral solubilities and local atomic structures of solutes have been reported on relatively simple systems containing a mineral and an aqueous fluid phase (e.g., quartz-H_2O, Zotov and Keppler, 2002; GeO_2–H_2O, Pokrovski et al., 2005a; Sb_2O_3–H_2O–NaCl–HCl, Pokrovski et al., 2006a, 2008b; Au–H_2O–H_2S–NaOH, Schott et al., 2006).

The present study focuses on in situ X-ray absorption spectroscopy measurements of gold speciation, solubility and structure in Cl-bearing aqueous fluids to 500 °C and 600 bar in the model systems $Au_{(s)}$–$HAuCl_4$–NaCl–HCl and $Au_{(s)}$–NaCl–H_2SO_4. Here we combined in situ XAFS experiments with quantum-chemical optimizations of complex geometries and calculations of near-edge X-ray absorption (XANES) spectra to investigate the stability, transformation kinetics, and structure of the principal Au^{III} and Au^{I} chloride complexes. Our results provide the first direct structural evidence for the $AuCl_2^-$ species in hydrothermal solution and demonstrate the promising potential of combining in situ synchrotron radiation spectroscopy with ab-initio modeling for in situ studies of complex high *T–P* fluid systems pertinent to Earth's hydrothermal-magmatic settings.

2. Materials and methods

2.1. Experimental design and XAFS spectra acquisition

Three types of aqueous solutions were examined in this study: $HAuCl_4$–NaCl–HCl, $Au_{(s)}$–$HAuCl_4$–NaCl–HCl, and $Au_{(s)}$–2 m NaCl–0.5 m H_2SO_4. Metallic gold foil was 0.5 mm thick with a purity of 99.99% (GoodFellow). Gold tetrachloride solution ($HAuCl_4$) was prepared by dissolving Au metal in 20% HCl boiling solution. Experimental solutions were prepared from analytical-grade reagents NaCl, HCl, H_2SO_4 and doubly de-ionized water.

XAFS spectra (including the X-ray absorption near edge structure region or XANES, and the extended X-ray absorption fine structure region or EXAFS) of aqueous Au solutions were collected in both transmission and fluorescence mode at the Au L_3-edge (~11.9 keV) over the energy range 11.7–13.0 keV on BM30B-FAME beamline (Proux et al., 2005) at the European Synchrotron Radiation Facility (ESRF, Grenoble, France). The storage ring was operated at 6 GeV with a ~180 mA current. Energy was selected using a Si(220) double-crystal monochromator with sagittal focusing. Contributions of higher-order harmonics from the Si(220) double-crystal within the FAME optics configuration do not exceed 0.1% of the transmitted intensity in the energy and absorbance ranges of our experiments (Proux et al., 2006). The beam size was focused to 300 μm horizontal ×200 μm vertical yielding an X-ray photon flux on the sample of ~10^{12} photons/s as measured with a calibrated Canberra diode. Silicon diodes collecting scattered radiation from a Kapton foil were employed for measuring the intensities of the incident (I_0) and transmitted (I_1 and I_2) X-ray beams while fluorescence spectra were collected in the 90° geometry using a Canberra solid-state 30-element germanium detector (energy resolution = 300 eV, shaping time = 125 ns). Energy was constantly calibrated using a gold metal foil placed behind the sample (i.e., between the I_1 and I_2 transmission detectors); its L_3 edge energy was set at 11.919 keV as the maximum of the first derivative of the main edge spectrum.

XAFS measurements were carried out using a spectroscopic cell recently described in detail elsewhere (Pokrovski et al., 2005a, 2006a; Testemale et al., 2005). Very briefly, the design includes an inner optical cell (Fig. 1) which is inserted in a high-pressure steel vessel pressurized with helium and having three beryllium windows for X-ray passage. The internal cell consists of a vertically oriented sapphire or glassy-carbon tube polished inside, and two sapphire coaxial rods equipped with Viton O-ring seals and inserted into the tube from each end. The rods delimit the sample space, in which experimental solid and solution are placed, and can move in the tube in response to pressure changes like a piston in a syringe. The volume of the sample space is about 0.1 to 0.2 cm^3 which corresponds to a height of 3 to 6 mm, depending on *T–P* conditions. Pressure in the sample space is always balanced with that of helium gas and the mobile pistons. The optical path through the vertically oriented cell remains constant owing to the low temperature expansion coefficient of sapphire and glassy carbon. The temperature in the sample space is maintained to ± 0.2 °C by Mo heating resistances and Pt–Pt/Rh thermocouples connected to a Eurotherm® temperature controller. Temperature gradients through the sample space do not exceed 5° at a run temperature of 400 °C. The Viton O-rings are situated outside the heating zone (at <100 °C when the sample-space temperature is 400 °C) to avoid their thermal degradation. This results in a relatively small 'dead-volume' space between the rods and glassy-carbon tube (<20–30% of the total cell volume) that produces minimal solute diffusion and solid precipitation below or above the hot sample space. Helium pressure is monitored using three pressure sensors placed at the cell exit and at the end of the pressure line. Pressure variations between them do not exceed 10 bars; the mean value is adopted. The cell design permits operation up to ~500 °C and ~2000 bar (depending of the amplitude of the fluid expansion and the thickness of Be windows). Additional details about the cell properties and operation limits are given in Pokrovski et al. (2006a).

It should be noted that because of the high external pressure coupled with elevated mobility of helium, partial diffusion of He into the internal cell and its dissolution in aqueous solution cannot be completely avoided. Such effects are expected to be weak at temperatures below 300 °C and experimental He pressures of 600 bar, at which He solubility in water ranges from 0.3 to 4 mol% between 25 and 300 °C as shown by thermodynamic calculations using available Henry constants (e.g., Schulte et al., 2001). However, its solubility might become important at near-critical temperatures, significantly lowering water activity and thus affecting solid phase solubilities. Measurements of He diffusivity into an empty cell through Viton seals at ambient temperature and He pressures above 500 bar

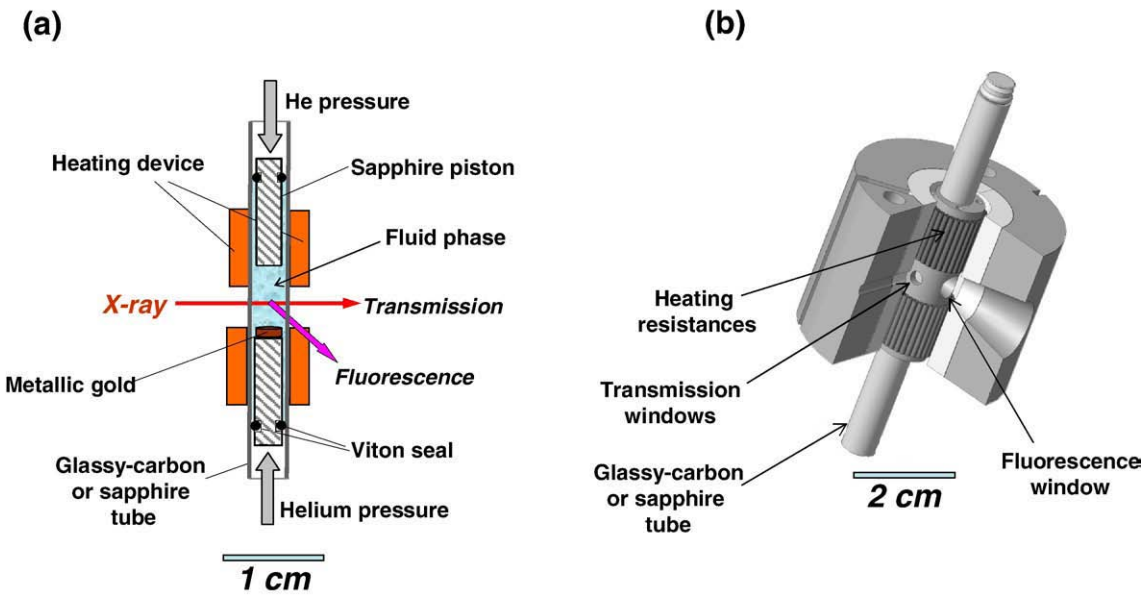

Fig. 1. (a) Details of the internal part of the X-ray cell, and (b) the assembled cell with a heating device used for XAFS measurements in this study.

demonstrated negligible He diffusion within the duration of typical XAFS experiments (1–2 days). Although it is difficult to quantitatively estimate the amplitude and rate of He diffusion at elevated *T*–*P* into the cell in the presence of a fluid phase, tests involving rapid cell cooling (<15 min) from 450 to 20 °C under 600 bar of He pressure revealed neither changes in the mass of fluid initially loaded nor the appearance of a vapor phase, thus indicating that He dissolution is likely to be insignificant in most experiments. Furthermore, previous solubility measurements in different systems at temperatures above 300 °C using the same cell design demonstrated excellent agreement with solubility data obtained in batch hydrothermal reactors (e.g., GeO_2–H_2O, Sb_2O_3–NaCl–HCl, Au–NaOH–S, Pokrovski et al., 2005a, 2006a,b, 2008b), thus implying that He dissolution in the experimental fluid (if occurs) has no significant effect on mineral solubilities and solute atomic structures.

A small piece of Au foil (~50 mg, 3 mm in diameter) was placed at the bottom of the sample space (i.e., on the top of the lower sapphire rod) below the beam passage through the aqueous solution. Note that the diameter of the holes (2–3 mm) in the heating assemblage around the cell tube is such that the Au solid at the cell bottom is never

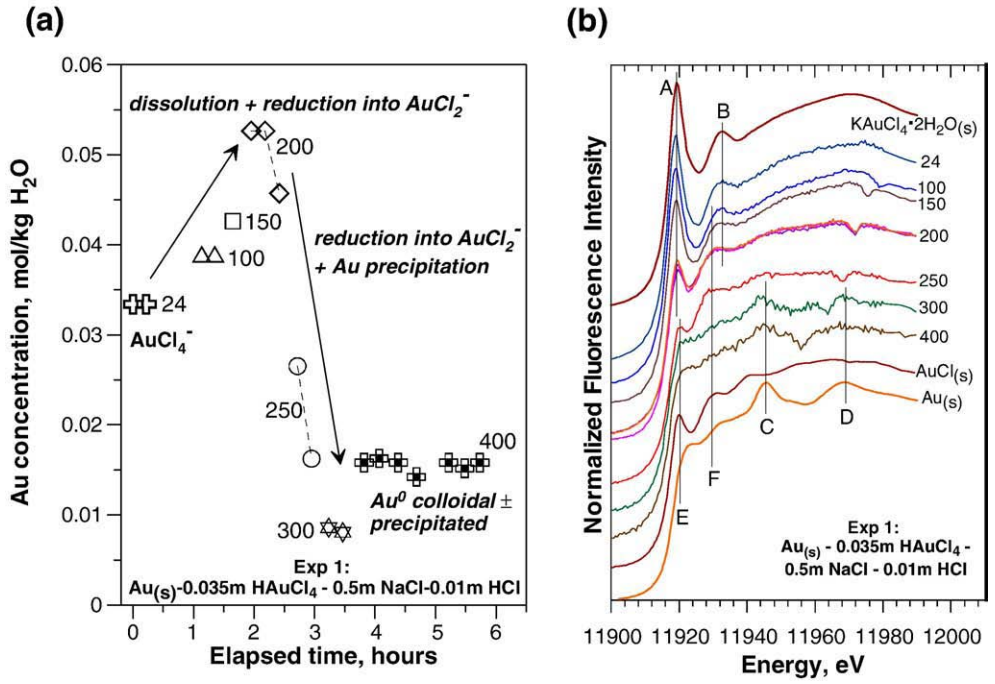

Fig. 2. (a) Evolution of dissolved Au concentration in solution at 600 bar in a mono-crystalline sapphire cell as a function of temperature and time in the system $Au_{(s)}$–$HAuCl_4$–NaCl–HCl for indicated composition and temperatures (in °C), measured by monitoring the absorption edge height in transmission mode. The error is comparable to the symbol size. (b) Normalized Au–L_{III} near-edge (XANES) spectra from the same experiment at indicated temperatures. Vertical lines show features characteristic of the square $AuCl_4^-$ species similar to those in crystalline $KAuCl_4 \cdot 2H_2O$ (A, B), metallic gold (C, D), and the linear [Cl–Au–Cl] unit in $AuCl_{(s)}$ and $AuCl_2^-$ complex (E, F). The glitches apparent in some spectra of solutions between 11,950 and 11,990 eV correspond to diffraction peaks from the sapphire cell walls. The spectrum of $AuCl_{(s)}$ was kindly provided by Doonan and Reith (personal communication).

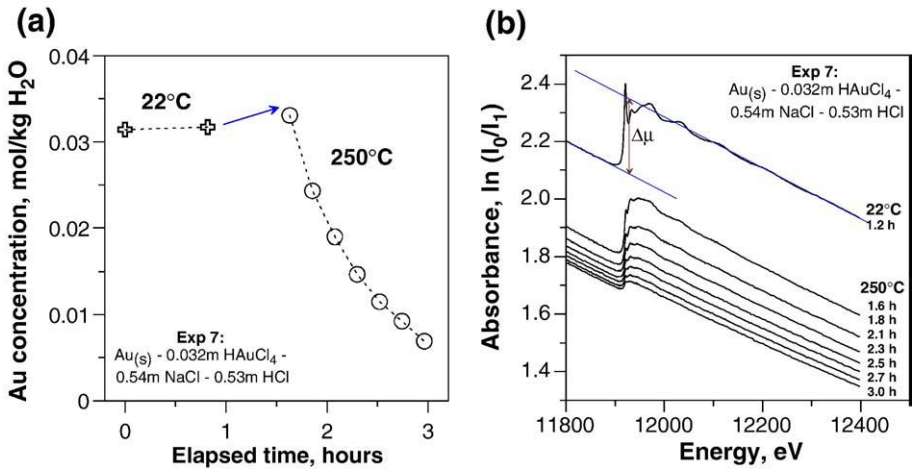

Fig. 3. (a) Evolution of Au dissolved concentration as a function of time in an acid $HAuCl_4$–NaCl–HCl aqueous solution of indicated composition in the presence of native gold (Exp 7), determined from the absorption edge height, Δμ, of the transmission spectra shown in (b), and using Eq. (1). The error is comparable to the symbol size. (b) Raw transmission scans at Au–L_{III} edge at 22 and 250 °C and 600 bar for the same experiment, as a function of run duration (in hours from the start of the experiment). The decrease of the total absorbance and absorption edge height at 250 °C demonstrates the precipitation of Au from solution.

exposed to the direct beam which "sees" only the central part of the sample space occupied by the fluid phase (Fig. 1). The cell was pressurized to 600 bars and heated. XAFS spectra were recorded at temperatures from 20 to 500 °C (depending on experiment and solution composition) and as a function of time, allowing the dissolved Au concentration and structural changes to be monitored (e.g., Figs. 2 and 3). The spectral amplitudes both in the XANES and EXAFS regions recorded in transmission and fluorescence modes were found to be identical demonstrating the absence of self-absorption effects in the fluorescence mode, at least at the investigated gold concentrations (≤~0.05 m).

2.2. XAFS spectra analysis

Classical EXAFS spectra reduction was performed with the Athena and Artemis packages (Ravel and Newville, 2005) based on the IFEFFIT program (Newville, 2001). Details about the reduction procedure can be found elsewhere (Pokrovski et al., 2005a, 2006a). Briefly, spectra were normalized to the absorption edge height, background-removed using the AUTOBK algorithm, weighted by k^n, where $n=1$, 2 or 3, and Fourier filtered over the k range from ~3 to 9–12 $Å^{-1}$ (depending on the signal-to-noise ratio) to produce radial structure functions (RSF). Fits were performed in R-space on both the real and imaginary parts of the RSF contributions (Newville, 2001) to obtain the identity of the backscattering atoms, Au-neighbor distance (R), coordination number (N), and the Debye–Waller factor (σ^2) for each scattering path. In addition to these structural parameters, a single nonstructural parameter, Δe, was varied to account for its estimate made by FEFF. To diminish correlations between N and σ^2, and R and Δe, and better account for light versus heavy neighbors and multiple scattering paths, fits were performed simultaneously with k-weightings of 1, 2 and 3. The fitted values of the structural parameters were identical within errors, with similar fit qualities for each k-weighting. This is an additional demonstration of both the validity of the chosen structural models and the accuracy of the EXAFS background removal procedures (Ravel and Newville, 2005). Theoretical backscattering amplitude and phase-shift functions for Au–Cl, Au–O, Au–H, Au–Na/K, Au–Au single and multiple scattering paths were computed using the FEFF6 *ab initio* code (Zabinsky et al., 1995) with Au, AuCl, Au_2O_3, $NaAuCl_4$, $KAuCl_4 \cdot 2H_2O$, and $Na_3Au(S_2O_3)_3 \cdot 2H_2O$ crystal structures. The amplitude reduction factor (S_0^2) was set at 0.85±0.05 as found by fitting spectra of these solid references. This value is identical to that reported previously for Au L_2 and L_3 edges of different compounds (Benfield et al., 1994). The influence of anharmonic disorder in determining structural parameters was checked using the cumulant expansion method (e.g., Crozier et al., 1988). The values of third- and fourth-order cumulants (c_3 and c_4) found when fitting the Au first coordination shell always converged to zero within errors ($\pm 10^{-4}$) and thus had no influence on the main structural parameters (R, N and σ). The presence of multiple scattering (MS) events within the Au first coordination shell was examined using the FEFF code (see below), assuming local D_h or C_{4v} geometries around Au, as found in the model compounds investigated. Multi-electron excitations (MEE) in the Au L_3-edge EXAFS region, like 2p4f which yields additional transitions at k ~4–6 $Å^{-1}$, may interfere with standard background subtraction procedures and thus influence the analysis (e.g., Benfield et al., 1994). However, these MEE could not be detected unambiguously in most of our Au^I spectra, in agreement with previous findings that showed a negligible impact of these transitions on EXAFS-derived structural parameters for Au^I-bearing compounds (Benfield et al., 1994; Berrodier et al., 2004). For Au^{III} samples, the MEE were identified in the spectra, but were found to be too weak to affect the structural parameters. In addition to the classical EXAFS analysis, XANES spectra of different Au aqueous species potentially present in the experimental solutions were modeled based on species optimized geometries generated using quantum-chemical algorithms and the EXAFS derived Au-ligand distances (see Section 2.4).

2.3. Determination of dissolved Au concentration from the absorption edge height

Dissolved Au concentrations were determined from the amplitude of the absorption edge height over the Au L_3-edge of transmission spectra ($\Delta\mu$) using the following equation based on the classical X-ray absorption relation (see Pokrovski et al., 2005a, 2006a; Testemale et al., 2005 for details):

$$C_{Au} = \Delta\mu / (\Delta\sigma_{Au} \times M_{Au} \times l \times d_{fluid}) \quad (1)$$

where C_{Au} is Au aqueous concentration (mol kg^{-1} of fluid), $\Delta\sigma_{Au}$ is the change of the total absorption cross-section of Au over its L_3-edge (cm^2 g^{-1}), l is the optical path length inside the cell (cm) which remains constant through the experiment, M_{Au} is Au atomic weight (0.1970 kg mol^{-1}), and d_{fluid} is the density of the aqueous solution (g cm^{-3}) at given T and P.

The absorption cross-sections for Au were taken from the recent compilation of Elam et al. (2002). These values are in close agreement, within ~5% below and above the Au L_3-edge, with other databases

(e.g., as compiled in the Hephaestus software, Ravel and Newville, 2005). In the absence of direct volumetric data on the system H_2O–NaCl–HCl–H_2SO_4–Au at elevated *T*–*P*, the fluid density in our XAFS experiments was approximated using the Pressure–Volume–Temperature–Composition (PVTX) properties of the system NaCl–H_2O (Anderko and Pitzer, 1993; Bakker, 2003), and assuming that Au/HCl/H_2SO_4 solutes in water yield the same contribution to the fluid density as the equivalent *weight concentration* of NaCl. It is expected that the maximum error of density estimations using this approximation does not exceed 10% at temperatures above 200 °C.

The height of the absorption-edge step ($\Delta\mu$) in each transmission EXAFS scan was determined using a classical 'empirical' normalization technique of the AUTOBK algorithm (Newville, 2001), and an independent Cromer–Liberman normalization (CLnorm, Cromer and Liberman, 1970), both implemented in the Athena software. Values of $\Delta\mu$ found using both approaches were identical within errors, thus confirming the validity of estimates of atomic-like background over the Au L_3-edge. The uncertainty on $\Delta\mu$ determinations, as estimated by changing fitted energy ranges or by comparing different scans for the same Au concentration, is less than 5% for a $\Delta\mu$ amplitude greater than 0.1 (~0.01 m Au), is about 10% for $\Delta\mu$ between 0.01 and 0.1, and reaches 30–50% for $\Delta\mu$ between 0.01 and 0.001 (~10^{-3}–10^{-4} m Au).

2.4. Quantum-chemical calculations of optimized structures and XANES spectra for Au aqueous species

The quantum chemical calculations were performed using the Gaussian 03 program (Frisch et al., 2004) based on Density Functional Theory (DFT) and second order Møller–Plesset (MP2) methods. DFT calculations were carried out using a B3LYP functional (Lee et al., 1988; Becke, 1993) incorporated into Gaussian 03. The 6-311+G(d) basis set was used for Cl, O, and H. The Stuttgart–Dresden (SDD) relativistic effective core potential (RECP) adopted in Schwerdtfeger et al. (1989) was used in most calculations for Au. This potential, combined with [7s-3p-4d] contraction for valence electrons, was used to approximate the Au inner electronic structure consisting of 60 electrons ([Kr]+4d+4f). Previously, the SDD RECP was successfully used to study structures and thermo-chemical properties of $Au^+(H_2O)_n$ clusters (Feller et al., 1999). We denote these theory levels as B3LYP/SDD/6-311+G(d) and MP2/SDD/6-311+G(d) for DFT and MP2 methods, respectively. In addition, a series of calculations for $AuOH(OH_2)^0$ and $AuCl_2^-$ was performed with the LANL2DZ (Hay and Wadt, 1985) and CEP-121G (Stevens et al., 1992) effective core potentials. Besides, to account for the effect of bulk solvent (water at 25 °C, ε=78.36), several calculations were carried out with the aid of a Polarized Continuum Model (PCM/B3LYP/SDD/6-311+G(d) theory level). The normal mode analysis showed that the calculated geometries represent the true minima on the potential energy surface.

XANES spectra of different Au aqueous species were modeled based on the optimized geometries of the predicted species and experimental EXAFS-derived Au-ligand distances, using the FDMNES computer code (Joly, 2001). This program calculates theoretical XANES spectra using two different formalisms, the classical multiple scattering (MS) muffin-tin method (e.g., Rehr et al., 1992) and/or the Finite Difference Method (FDM) where the electron potential is calculated by resolving the Schrödinger equation on the node points of a three-dimensional grid (Kimball and Shortley, 1934). The obtained raw calculations represent the evolution of the photo-absorption cross-section of Au as a function of X-ray photon energy and correspond to the transition amplitude between the initial and final states. The generated raw spectra, which correspond to an energy resolution of the FD method (<0.1 eV) and thus display almost all possible electronic transitions, are further convoluted with a Lorentzian function with a full width Γ_h of 5.41 eV to account for the core hole lifetime at the Au L_3-edge, and a Gaussian function to account for the experimental resolution assumed to be equal to the intrinsic resolution of the monochromator (Γ_{exp}=0.61 eV, Proux et al., 2006). The convolution parameters were fixed in all subsequent analyses. Because the electronic states below the Fermi level are occupied, the absorption cross section is taken to be equal to zero below the Fermi energy prior to the convolution. All calculations were performed in the FDM mode in order to test different clusters symmetries and geometric configurations (note that in case of low symmetry, the muffin-tin approximation is not sufficient in the near-edge energy range; Joly, 2001). The values of energy for the Fermi level were fixed to −4.0 and −2.9 eV for Au^{III} and Au^{I}, respectively, as deduced from examination of the density of state (DOS) evolution of the different electronic states.

3. Results

3.1. Evolution of XANES spectra and gold dissolved concentrations in Au^{III}/Au^{I} acidic chloride solutions

3.1.1. $HAuCl_4$–NaCl–HCl system

Two experiments in a glassy-carbon and mono-crystalline sapphire cell were performed on an aqueous solution of the initial composition ~0.035 m $HAuCl_4$–0.50 m NaCl–0.01 m HCl at temperatures to 300 °C and pressures of 600 bar (Exp 2 and 3, Table 1). Aqueous gold concentrations derived from transmission spectra by monitoring the absorption edge amplitude as a function of temperature and time are reported in Table 1. It was found that in the carbon cell dissolved Au concentrations remain stable to 100 °C, but decrease rapidly at $T \geq 150$ °C both with time at the same *T* and with increasing *T*, whereas in the sapphire cell Au concentrations are identical to the initial value at $T \leq 250$ °C, at least within the time interval passed at each temperature (20 to 80 min, see Table 1). XANES spectra of these solutions (Fig. 4) are the same at $T \leq 100$ and identical to those of crystalline Na and K auric chlorides ($NaAuCl_4$, $KAuCl_4 \cdot 2H_2O$) and acidic (pH ≤ ~5) $HAuCl_4$-bearing solutions over a wide range of Au (10^{-5}–10^{-1} m) and chloride (0.01–1 m) concentrations at ambient *T*–*P* reported previously by Berrodier et al. (2004) and Farges et al. (1993). As shown in detail in these works, the XANES spectra of these compounds are dominated by a strong pre-edge feature at ~11919 eV arising from electronic transitions from the 2p ground states to the partially empty 5d states of Au^{3+} (Berrodier et al., 2004). The spectra of aqueous Au^{III} in acidic chloride media below 100 °C recorded in our study are fully consistent with the dominant presence of the square-plane $AuCl_4^-$ complex, in agreement with these XAFS and other independent low-temperature Raman and UV–Vis data (Pan and Wood, 1991; Peck et al., 1991; Murphy et al., 2000).

At temperatures above 150 °C, both in carbon and sapphire cells, the amplitude of the Au^{III} pre-edge feature decreases rapidly with temperature and time, and the shape of XANES spectra indicates the precipitation of metallic gold at $T \geq 200$ °C (Fig. 4). However, the fast spectral evolution together with rapid decrease of Au concentration did not allow accurate assessment of all spectral features within the limited beam time. The major conclusion from these experiments is the instability of $AuCl_4^-$ at temperatures above 150 °C, resulting in rapid transformation to other species followed by metallic gold precipitation. These phenomena are much faster in the carbon cell than the sapphire cell since C is likely to create reducing conditions favorable to Au^{III} reduction. A more quantitative assessment of Au^{III} reduction processes has been obtained from experiments in the presence of metallic gold reported below.

3.1.2. $Au_{(s)}$–$HAuCl_4$–NaCl–HCl system

Two experiments were performed in a carbon and sapphire cell on the same initial solution composition as above but in the presence of a piece of metallic Au placed in the cell together with the Au^{III} chloride solution (Exp 1 and 4, Table 1). A third experiment was done in a polycrystalline sapphire cell at more acidic conditions and higher Cl concentrations (Exp 7, $Au_{(s)}$–0.032 m $HAuCl_4$–0.54 m NaCl–0.53 m

Table 1
Total dissolved gold concentrations and fraction of the $AuCl_2^-$ species in aqueous solution in the systems $HAuCl_4$–NaCl–HCl, $Au_{(s)}$–$HAuCl_4$–NaCl–HCl, and $Au_{(s)}$–NaCl–H_2SO_4 at 600 bar as a function of temperature, run duration, and cell material

Run/cell	System composition (mol/kg H_2O)	T, °C	Time, hours	m_{Au}	$AuCl_2^-$, mol%
Exp 2 sapphire	0.036 m $HAuCl_4$–	24	0.2	0.037	0
	0.50 m NaCl–	100	1.2	0.036	<3
	0.01 m HCl	150	0.7	0.036	<3
		200	0.3	0.037	24±2
		250	0.3	0.037	86±4
		300	2.4	0.03–0.01	95±5
Exp 3 carbon	0.036 m $HAuCl_4$–	30	1.6	0.036	<4
	0.50 m NaCl–	100	1.4	0.036	10±2
	0.01 m HCl	150	1.4	0.035–0.031	43±3
		175	1.4	0.027–0.015	78±5
		200	1.4	0.008–0.002	Au^0
		225	1.4	<0.002	Au^0
		250	1.0	<0.002	Au^0
Exp 7 sapphire	Au–	22	1.2	0.032	0
	0.032 m $HAuCl_4$–	250	1.9	0.033–0.007	100
	0.54 m NaCl–				
	0.53 m HCl				
Exp 1 sapphire	Au–	24	0.7	0.033	<3
	0.035 m $HAuCl_4$–	100	0.8	0.039	9.5±3
	0.50 m NaCl–	150	0.3	0.043	29±2
	0.01 m HCl	200	0.8	0.053–0.046	73±2
		250	0.5	0.027–0.016	97±2
		300	0.6	~0.009	Au^0
		400	2.1	~0.015	Au^0
Exp 4 carbon	Au–	30	1.9	0.037	<3
	0.036 m $HAuCl_4$–	100	2.0	0.039–0.037	14±2
	0.50 m NaCl–	150	2.0	0.039–0.033	41±3
	0.01 m HCl	200	2.6	2.4×10^{-2}–5×10^{-4}	Au^0
		250	0.6	$<5\times10^{-4}$	Au^0
Exp 5 carbon	Au–2.6 m NaCl–	300	0.8	$\leq10^{-5}$	>95
	0.53 m H_2SO_4	400	0.7	$\leq5\times10^{-5}$	>95
		450	0.7	$\sim2\times10^{-3}$	>95
Exp 6 carbon	Au–2.6 m NaCl–	400	1.4	$\leq2\times10^{-4}$	>95
	0.53 m H_2SO_4	500	3.4	$\leq3\times10^{-4}$	>95

$AuCl_2^-$ mole fraction was derived using linear combination analysis (LCA) of normalized XANES spectra which was performed in the range −30 to 60 eV over the Au L_{III}-edge and using the spectra from Exp 7 at 22 and 250 °C as the references for the $AuCl_4^-$ and $AuCl_2^-$ species, respectively, and assuming that $Au_{tot} = AuCl_4^- + AuCl_2^-$.
Au^0 means that almost all Au was lost from solution and metallic gold precipitated, the gold remaining in solution is likely to be in the colloidal form and/or deposited on the cell optical windows.
m_{Au} = total dissolved Au molality derived from the absorption edge amplitude in transmission mode and using Eq. (1), a concentration range denotes the initial and final m_{Au} value at the given T.
Time represents the duration of spectra acquisition (in hours) at each temperature step.

HCl). The run in the carbon cell (Exp 4) yielded similar results to those described above showing a systematic (though somewhat slower than without the metal) decrease of both the Au^{III} pre-edge feature and dissolved Au total concentrations at 100–150 °C, followed by rapid Au precipitation at 200–250 °C (see Fig. 4 for similar experiments).

In contrast, the same run performed in the sapphire cell (Exp 1) showed a higher thermal stability of the studied solution, with significant increase of Au concentrations from 0.035 m (at 30 °C) to a maximum value of 0.053 m with rising temperature to 200 °C (Fig. 2a). Gold dissolution was accompanied by systematic changes in the XANES spectra as manifested by i) a decrease of the Au^{III} pre-edge peak amplitude and ii) energy shifts of the main $Au^{III}Cl_4$ XANES features (identified as A and B in Fig. 2b). At 200 °C, Au concentrations were found to decrease slightly (by ~20%) within an hour, whereas the XANES spectra of three successive scans remained almost identical (Fig. 2b). At 250 °C, Au precipitation was accelerated (Fig. 2a), but successive XANES scans (20 min each) did not show changes within the experimental resolution. At this temperature, the XANES spectra are characterized by a weak resonance at ~11921 eV (feature E) which is different in energy from the Au^{III} pre-peak (feature A at 11919 eV), and by another resonance at 11929 eV (feature F) not present in the spectra of Au^{III} at $T \leq 100$ °C (Fig. 2b). Note that a linear combination of Au^{III} and Au^0 spectra could not account for these resonances. These features are very close to those of the XANES spectrum of crystalline $AuCl_{(s)}$ in which Au is linearly coordinated with two Cl atoms (Straehle and Loercher, 1974). The EXAFS part of these spectra could not be examined, however, due to the presence of numerous diffraction peaks arising from the mono-crystalline sapphire tube. At higher temperatures (300 and 400 °C), an extremely rapid (within ~10 min, corresponding to the time necessary to raise temperature) Au precipitation occurred and XANES spectra displayed the major features of metallic gold (features C and D in Fig. 2), without detectable evolution with time (up to 2 h). The gold remaining in solution (<0.01 m) might be present in colloidal form, but some contribution to the spectra from the metal deposited on the cell walls in front of the transmission and fluorescence windows cannot be ruled out. This experiment thus demonstrated that Au^{III} reduction, likely into soluble Au^I chloride complexes, occurs in a limited temperature window (150–250 °C).

A third experiment, carried out at 250 °C for a longer duration in a more acidic and Cl concentrated solution (0.53 m HCl, 0.54 m NaCl, Exp 7) using a poly-crystalline sapphire cell with more tightly adjusted pistons and smaller dead volume (<10% of cell volume), confirms these findings. It can be seen in Fig. 3 that, although total Au concentrations decrease systematically with time, normalized XAFS spectra recorded in successive scans over about 2 h do not show any detectable evolution. They are identical within normalization errors to those recorded at 250 and 300 °C in the other sapphire-cell experiments described above (Exp 1 with $Au_{(s)}$ and Exp 2 without

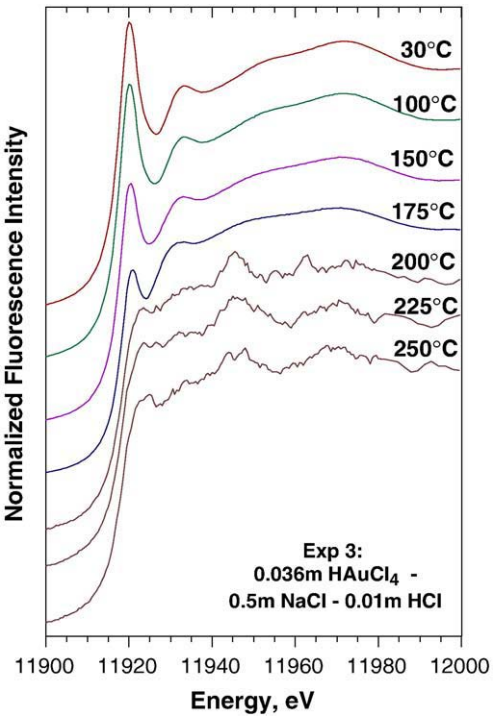

Fig. 4. Normalized Au–L_{III} XANES spectra from Exp 3 in a carbon cell (0.036 m $HAuCl_4$–0.50 m NaCl–0.01 m HCl) at 600 bar and indicated temperatures (spectra at each T are shifted along the vertical axis for clarity). The spectrum at each temperature is the sum of 2 to 3 scans (30 min each) that show only a weak evolution with time. Spectra at $T \geq 200$ °C correspond to gold metal, whereas those recorded between 30 and 175 °C are likely to be a mixture of Au^{III} and Au^I chloride species. The high noise of the gold metal spectra is due to the low Au concentration in solution (m_{Au}<0.01, see Table 1). Identical spectra were recorded in Exp 4 in a carbon cell ($Au_{(s)}$–0.036 m $HAuCl_4$–0.50 m NaCl–0.01 m HCl) from 30 to 150 °C (not shown).

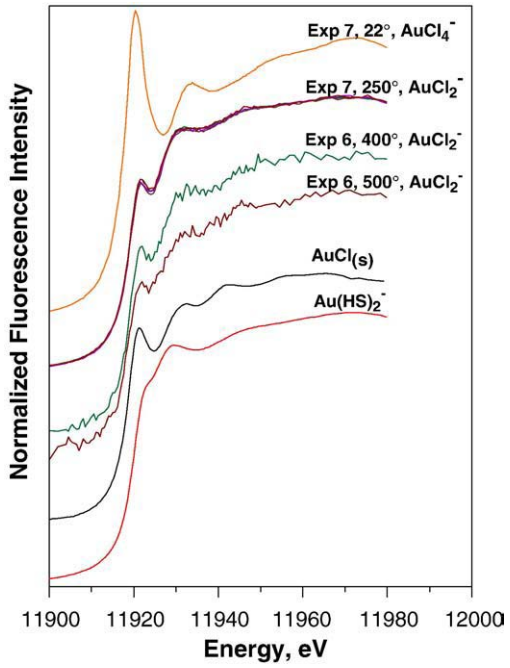

Fig. 5. Normalized Au–L_{III} XANES spectra from selected solutions in the presence of native gold at 600 bar and indicated temperatures (spectra at each *T* are shifted along the vertical axis for clarity): Exp 7 = $Au_{(s)}$–0.032 m $HAuCl_4$–0.54 m NaCl–0.53 m HCl, Exp 6 = $Au_{(s)}$–2.6 m NaCl–0.53 m H_2SO_4. In Exp 7 at 250 °C several scans recorded at different times are presented (see Fig. 3), they show no detectable evolution with time. The spectra of crystalline $AuCl_{(s)}$, and the linear $Au(HS)_2^-$ complex at 300 °C/600 bar (Schott et al., 2006), analogous to $AuCl_2^-$, are also shown for comparison. The poor statistics of the spectra in Exp 6 is due to the low Au solution concentration (~10^{-4} m, see Table 1).

$Au_{(s)}$). It is thus very likely that at elevated temperatures $AuCl_4^-$ reduces into Au^I-Cl complexes, presumably $AuCl_2^-$, as suggested both from in situ Raman spectroscopy on similar solutions (Pan and Wood, 1991; Murphy et al., 2000) and solubility measurements in the system $Au_{(s)}$–$Au^{III}Cl_4$–NaCl–HCl (Gammons and Williams-Jones, 1995, 1997), which showed that increasing the temperature in the presence of metallic gold promotes the reduction of $AuCl_4^-$ into $AuCl_2^-$ according to

$$2Au_{(s)} + AuCl_4^- + 2Cl^- = 3AuCl_2^- \quad (2)$$

3.1.3. $Au_{(s)}$–NaCl–H_2SO_4 system

Two runs were performed to study Au dissolution in a 2.6 m NaCl–0.53 m H_2SO_4 solution at temperatures from 300 to 500 °C at 600 bar using a carbon cell (Exp 5 and 6). Dissolved gold concentrations were found to be close to the detection limit of our technique (<10^{-3}–10^{-4} m Au) and showed no detectable evolution with time, over at least 3 h (see Table 1). Despite the significant noise affecting the XANES spectra recorded from these Au-poor solutions (Fig. 5), their main features were found to be very similar to those in the Au^{III}–Cl ± $Au_{(s)}$ systems at 250 °C and lower Cl concentrations described above. Equilibrium thermodynamic calculations carried out using the available stability constants for $Au^{III}Cl_4^-$ and Au^I chloride and hydroxide complexes (see Appendix) indicate that $AuCl_2^-$ should be by far the dominant Au species in the experimental solutions, with concentrations increasing from 0.001 to 0.1 m Au between 300 and 500 °C. The much lower Au concentrations measured by XAFS in this study are likely due to the presence of carbon whose partial dissolution at *T*>300 °C generates more reducing conditions than those predicted for a NaCl–H_2SO_4 solution, and thus favors the stability of metallic gold. For example, calculations show that in Exp 5 at 300 °C in the presence of graphite, H_2S is the dominant sulfur species, pH becomes less acidic (pH ~3.9 versus ~1.0 without graphite), and Au concentrations decrease ~20 times (to ~3×10^{-5} m), whereas $AuCl_2^-$ largely dominates over $AuHS^0$ that forms in the presence of H_2S at acidic pH. A detectable H_2S smell after our experiments confirms these thermodynamic predictions. Thus, these experiments, together with those described above (Sections 3.1.1 and 3.1.2), provide a further confirmation that similar Au^I–Cl complexes, presumably $AuCl_2^-$, form in acidic chloride solutions over wide temperature (250–500 °C) and Cl concentration (0.5–2.6 m) ranges.

3.2. Local structure of Au chloride complexes in hydrothermal fluids

Normalized EXAFS spectra and their corresponding Fourier Transforms from selected solutions in the system $HAuCl_4$–NaCl–HCl with and without metallic Au obtained in a glassy-carbon or polycrystalline-sapphire cell (Exp 3, 4 and 7) are shown in Fig. 6 and the derived structural parameters are reported in Table 2. In both systems, the spectra at ≤30 °C and pressures 1 and 600 bars are identical and can be accurately modeled with 3.9±0.2 Cl atoms at an average distance of 2.282±0.004 Å around the gold atom, and a very weak thermal and/or structural disorder (DW factor ~0.001 $Å^2$). The pronounced feature apparent in the Fourier Transform Magnitude of these spectra at ~4 Å (not corrected for phase shift) corresponds to linear multiple scattering paths within the $AuCl_4^-$ cluster. This is supported by their fitted DW factors and path distances which are twice those for the single scattering Au–Cl paths. This feature is a direct indication that Cl atoms are arranged in square-plane geometry around the central Au atom, similar to the crystal structures of tetra-aurates of alkaline metals (e.g., Théobald and Omrani, 1980; Jones et al., 1988), thus confirming that $AuCl_4^-$ is by far the dominant species in our solutions, in full agreement with the previous findings from X-ray diffraction, Raman and XAFS spectroscopy (Maeda et al., 1974; Benfield et al., 1994; Murphy et al., 2000; Berrodier et al., 2004).

It can be seen in Fig. 6 that with increasing temperature the spectral amplitude decreases systematically consistent with quantitative EXAFS modeling which predicts both a decrease of the average number of Cl atoms and an increase of the Au–Cl DW factors which attain values of 1.8±0.3 atoms and ~0.002 $Å^2$, respectively, with a mean Au–Cl distance of 2.267±0.004 Å at 250 °C and 600 bar. Note that EXAFS spectra in experiments with and without metallic gold in the *T* range 20–150 °C (Exp 3 and 4) are identical and yield similar structural parameters (Table 2). No changes in spectra were detected below 100 °C demonstrating that the structure and Au–Cl distances in the dominant $AuCl_4^-$ complex do not change significantly at least in this *T*-range. At *T*≥150 °C, average Au–Cl distances exhibit a slight but detectable decrease (by ~0.01 Å, Table 2). This evolution is likely to reflect a decrease in the proportion of $AuCl_4^-$ versus $AuCl_2^-$ with rising temperature. The amplitude of the MS feature gradually decreases with temperature and is consistent with the multiple scattering paths within the linear Cl–Au–Cl unit, with values of *R*, *N* and σ^2 parameters twice as those for the single scattering Au–Cl path. The low DW factors, very weak evolution of Au–Cl distances with temperature, and negligible 3rd- and 4th-order cumulants from anharmonic analyses indicate very little thermal and positional disorder. This reflects the strong covalent character of Au–Cl bonds in gold-chloride complexes and weak interactions of AuCl species with the solvent water molecules (hydration). The weak-to-negligible evolution with *T* of the structural parameters for $AuCl_4^-$ and $AuCl_2^-$ species is similar to that observed for other strongly covalent and weakly hydrated complexes of soft metals (e.g., $As(OH)_3$, Pokrovski et al., 2002; Testemale et al., 2004; $Ge(OH)_4$, Pokrovski et al., 2005a; $Sb(OH)_3$, Pokrovski et al., 2006a; $Au(HS)_2^-$, Pokrovski et al., 2006b; Schott et al., 2006) whose molecular structure and stability are only slightly sensitive to the changes in the solvent density and dielectric constant (e.g., Pokrovski et al., 1999, 2005b, 2008a).

The EXAFS-derived parameters are in agreement with a progressive reduction of the fraction of $AuCl_4^-$ complexes with increasing temperature in both systems (i.e., with and without metallic Au), consistent with the evolution of the XANES spectra described above (Section 3.1). The

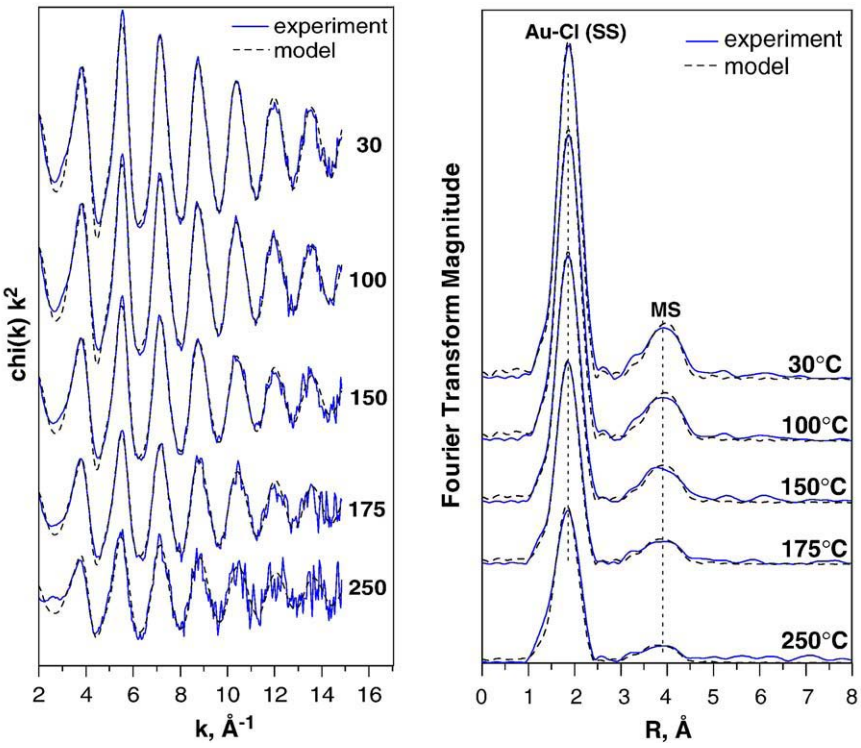

Fig. 6. Normalized k^2-weighted EXAFS spectra from Au-bearing NaCl–HCl aqueous solutions at 600 bar and indicated temperatures (in °C), and their corresponding Fourier Transform magnitudes (not corrected for phase shift). Dashed curves denote fits using the parameters from Table 2; vertical dotted lines indicate the position of Cl neighbors (corresponding to a single scattering path, SS) and linear multiple scattering paths (MS). Spectra at temperatures 30–175 °C are from Exp 3 and 4 with the starting composition 0.036 m $HAuCl_4$–0.50 m NaCl–0.01 m HCl, whereas the spectrum at 250 °C comes from Exp 7 with the starting composition $Au_{(s)}$–0.032 $HAuCl_4$–0.54 m NaCl–0.53 m HCl (see Table 1). The slight mismatch of the experimental spectra by the fit at ~4.5 and ~6.0 is likely to correspond to multi-electron transitions not accounted for by classical EXAFS modeling (Berrodier et al., 2004).

number of Cl neighbors derived from the spectrum at the highest temperature (250 °C) is likely to correspond to the dominant presence of the linear $AuCl_2^-$ complex which should represent at least 90% of the total dissolved Au at these conditions considering the uncertainties of the N_{Cl} values. No neighbors other than Cl (e.g., O, Na) could be detected around Au within the experimental resolution (~10%), suggesting that the sum of the fractions of Au^I hydroxide species (e.g., $AuOH(H_2O)^0$), the hydrated cation ($Au(H_2O)_2^+$), and Au^I and Au^{III} hydroxy-chloride complexes (e.g., $Au(H_2O)Cl^0$, $Au(OH)Cl^-$, $Au^{III}Cl_{4-n}(OH)_n$) is less than 10% of total dissolved Au at 250 °C. Because EXAFS sees the average atomic environment around the absorbing atom, the presence of some fraction of $AuCl_4^-$ or other eventual $AuCl_n$ complexes having no OH/H_2O ligands in the first Au coordination shell cannot be ruled out on the basis of EXAFS spectra only. Independent criteria from thermodynamics and XANES spectra help constrain the Au–Cl speciation model. The dominant presence of $AuCl_2^-$ in solutions above 200–250 °C is in agreement with the equilibrium thermodynamic calculations showing that this species accounts for more than ~70 and 85% of total Au at 250 °C in the systems $Au_{(s)}$–$HAuCl_4$–0.5 m NaCl–0.01 m HCl and $Au_{(s)}$–$HAuCl_4$–0.5 m NaCl–0.5 m HCl, respectively (Supplementary Table). Unlike EXAFS, XANES spectra are particularly sensitive to the absorber oxidation state and cluster symmetry and geometry. As it will be shown below, an independent demonstration that $AuCl_2^-$ is by far the dominant Au species at these conditions is provided by ab-initio XANES spectra modeling using the optimized species geometries calculated by quantum-chemical algorithms and the experimental EXAFS-derived Au–Cl distances.

Table 2
Average gold local atomic structure in aqueous solution in the systems $HAuCl_4$–NaCl–HCl and $Au_{(s)}$– $HAuCl_4$–NaCl–HCl, as a function of temperature, pressure and cell material, derived from fitting EXAFS spectra at Au–L_{III} edge

T, °C	*P*, bar	Atom	*N*, atoms	*R*, Å	σ^2, Å^2	$\mathcal{R}$-factor
Exp 7: $Au_{(s)}$–0.032 m $HAuCl_4$–0.54 m NaCl–0.53 m HCl, sapphire cell						
22	600	Cl	3.8	2.281	0.0010	0.016
250	600	Cl	1.8	2.267	0.0024	0.017
Exp 3: 0.036 m $HAuCl_4$–0.50 m NaCl–0.01 m HCl, carbon cell						
30	1	Cl	4.0	2.283	0.0012	0.010
30	600	Cl	3.9	2.282	0.0012	0.014
100	600	Cl	3.6	2.283	0.0016	0.007
150	600	Cl	3.0	2.279	0.0018	0.008
175	600	Cl	2.3	2.273	0.0020	0.006
Exp 4: $Au_{(s)}$–0.036 m $HAuCl_4$–0.50 m NaCl–0.01 m HCl, carbon cell						
30	600	Cl	3.9	2.283	0.0012	0.011
100	600	Cl	3.5	2.283	0.0016	0.010
150	600	Cl	3.0	2.280	0.0017	0.009
Error			±0.3	±0.004	±30%	

R = gold-backscatterer mean distance, *N* = coordination number, σ^2 = squared Debye–Waller factor (relative to σ^2 = 0 adopted in the calculation of reference amplitude and phase functions by FEFF), $\mathcal{R}$-factor defines goodness of the total fit in *R*-space as described in IFEFFIT (Newville et al., 2001). For all samples the fitted *k*- and *R*-ranges were respectively 3.0–11.0 Å^{-1} and 1.2–4.8 Å (not corrected for phase shift). Major multiple scattering contributions (MS) within the linear $AuCl_2$ and square plane $AuCl_4$ clusters like Au–Cl1–Cl2–Au ($R_{ms1} = 2 \times R_{Au-Cl}$), and Au–Cl1–Au–Cl2–Au ($R_{ms2} = 2 \times R_{Au-Cl}$) were included in all fits. Their DW factors were found to range between 0.002 and 0.004 Å^2. The number of variables in the fit, N_{var} = 4 to 7, number of independent points, N_{ind} ~ 17.

3.3. Quantum-chemical calculations of Au–Cl species structures and XANES spectra

The optimized Au–O and Au–Cl distances and bond angles for different Au hydroxide and chloride species are listed in Table 3, and selected complexes geometries are shown in Fig. 7. Calculations demonstrate that all Au^I complexes adopt linear configurations, whereas $AuCl_4^-$ has a planar square-like structure, in agreement with general chemical rules and available crystallographic data. The Au–Cl distances calculated at all theory levels are 0.05–0.1 Å longer than the experimental values. The use of different relativistic effective core potentials for Au yields Au–Cl and Au–O distances which agree with

Table 3
Au–O and Au–Cl bond lengths (in angstroms) and ligand–Au–ligand angles (in degrees) for Au–OH–Cl complexes predicted from quantum chemical calculations, and their comparison with EXAFS data

Species	Chemical bond	L–Au–L angle, calculated	*R*, calculated	R, EXAFS
$Au(OH)(H_2O)^0$, gas[a]	Au–OH	175.9	1.98	
	$Au–OH_2$		2.18	
$Au(OH)(H_2O)^0$, gas[b]	Au–OH	176.5	1.97	
	$Au–OH_2$		2.15	
$Au(OH)(H_2O)^0$, gas[c]	Au–OH	175.9	1.99	
	$Au–OH_2$		2.19	
$Au(OH)(H_2O)^0$, gas[d]	Au–OH	175.7	1.98	
	$Au–OH_2$		2.19	
$Au(OH)(H_2O)^0$, aq[e]	Au–OH	178.6	2.02	
	$Au–OH_2$		2.08	
$AuCl(H_2O)^0$, gas[a]	Au–Cl	179.7	2.28	
	$Au–OH_2$		2.19	
$AuCl(H_2O)^0$, gas[b]	Au–Cl	179.8	2.25	
	$Au–OH_2$		2.15	
$AuCl(H_2O)^0$, aq[e]	Au–Cl	178.8	2.33	
	$Au–OH_2$		2.15	
$AuCl_2^-$, gas[a]	Au–Cl	180.0	2.36	
$AuCl_2^-$, gas[b]	Au–Cl	180.0	2.32	
$AuCl_2^-$, gas[c]	Au–Cl	180.0	2.37	
$AuCl_2^-$, gas[d]	Au–Cl	180.0	2.38	
$AuCl_2^-$, aq[e]	Au–Cl	180.0	2.37	2.267±0.004
$AuCl_2^-\cdot 2H_2O$, gas[a]	Au–Cl	180.0	2.35	
$AuCl_4^-$, gas[a]	Au–Cl	90.0	2.37	
$AuCl_4^-$, gas[b]	Au–Cl	90.0	2.33	
$AuCl_4^-$, aq[e]	Au–Cl	90.0	2.37	2.282±0.004
$AuCl_4^-\cdot 4H_2O$, gas[a]	Au–Cl	90.0	2.36	

[a] B3LYP/SDD/6-311+G(d).
[b] MP2/SDD/6-311+G(d).
[c] B3LYP/CEP-121G/6-311+G(d).
[d] B3LYP/LANL2DZ/6-311+G(d).
[e] PCM/B3LYP/SDD/6-311+G(d).

one another within ~0.02 Å. The solvation of Au complexes by water molecules, with the formation of $AuCl_2^-\cdot 2H_2O$ and $AuCl_4^-\cdot 4H_2O$ gaseous clusters results in a small (by 0.01 Å) decrease of Au–Cl distances. Changes in $AuCl_2^-$ and $AuCl_4^-$ geometries induced by the incorporation of bulk solvent effects using the PCM model are also minor (≤0.01 Å, ≤1°). In contrast, solvation of polar molecules $Au(OH)(OH_2)^0$ and $AuCl(OH_2)^0$ results in elongation of Au–OH and Au–Cl distances (by 0.04 and 0.05 Å, respectively), and shortening of $Au–OH_2$ distances (by 0.10 and 0.04 Å for $Au(OH)(OH_2)^0$ and $AuCl(OH_2)^0$, respectively) compared to the gas phase geometries. These calculations are in qualitative agreement with those of Tossel (1996). Calculations at the MP2 level of theory yield shorter than DFT Au–Cl distances which are closer to those determined from EXAFS experiments, with differences of ~0.05 Å.

The calculated geometries of Au–Cl complexes and EXAFS-derived Au–Cl distances can be used to quantitatively interpret the XANES spectra obtained in this study (e.g., Fig. 2b). It should be remembered that the 'white line' observed in the XANES spectra of most Au^I and Au^{III} compounds results from the 2p to 5d orbital electronic transitions and should be regarded rather as a pre-edge feature (e.g., Benfield et al., 1994; Berrodier et al., 2004; references therein). In Au^{III} compounds like $KAuCl_4\cdot 2H_2O_{(s)}$, the 5d orbital is partially empty and such a transition yields a particularly intense feature (labeled A in Fig. 2b). In contrast, for Au^I compounds like $AuCl_{(s)}$, the amplitude of the 'white line' (labeled E in Fig. 2b) is dramatically decreased and slightly shifted to higher energy because only a single electron transition is allowed to the $5d^9$ orbital set. In the case of native gold $Au_{(s)}$, the 5d orbital is filled, having a d^{10} electronic configuration, thus rendering the 2p5d transition impossible. This leads to the disappearance of the 'white line' in its spectrum. Thus, the 'white line' feature allows direct determination of the oxidation state of Au in its aqueous and solid species, which is quantitatively confirmed by XANES ab-initio modeling.

XANES modeling was performed to check the two different model geometries suggested by quantum chemical calculations, i.e. square-plane $Au^{III}Cl_4$ and linear Au^ICl_2 structures, which are inferred for Exp 7 at 22 and 250 °C, respectively, on the basis of XANES spectra comparisons and EXAFS-derived distances and coordination numbers (see Sections 3.1 and 3.2). The calculations were performed for isolated molecules by taking into account only the central Au atom and the first shell composed of Cl atoms, without considering solvation effects in solution. The electronic structures of Au^0, Au^I

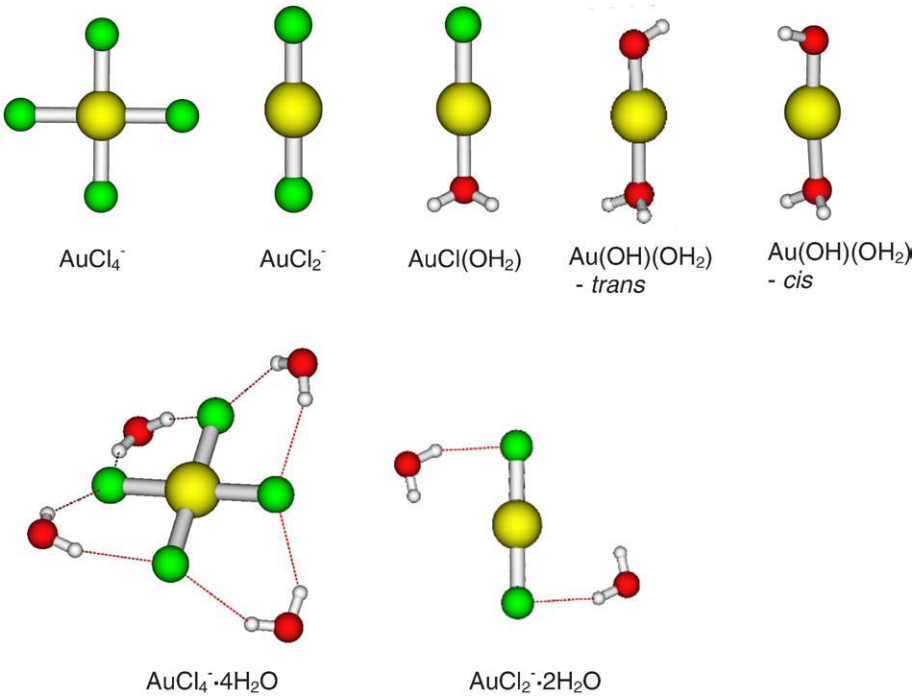

Fig. 7. Optimized gas-phase geometries of Au^{III} and Au^I chloride and hydroxide species calculated using DFT quantum-chemical methods using B3LYP/SDD/6-311+G(d) formalisms.

and Au^{III} were assumed to be respectively $[Xe]4f^{14}5d^{10}6s^1$, $[Xe]4f^{14}5d^96s^1$ and $[Xe]4f^{14}5d^86s^1$. Note that the partial charge on the gold atom is +1 for Au^I and +2 for Au^{III}, because the valence state electron is not completely delocalized, particularly in case of the strongly covalent Au^{III}–Cl compounds; this results in a lower partial charge on the Au^{III} atom than the apparent oxidation state of +3. Calculated and experimental spectra are compared in Fig. 8.

It can be seen that for both structures, the raw calculations reproduce all characteristic features observed in the experimental spectra. The convoluted spectrum for the $Au^{III}Cl_4$ cluster corresponds fairly well to the experimental one at 22 °C where $AuCl_4^-$ is by far the dominant species. For Au^ICl_2, the agreement is less good, particularly in the near-edge energy range. The calculated 'white' line position is shifted by ~2 eV to lower energy and exhibits a lower amplitude compared to the experimental spectrum. However, all major features in the 20–60 eV range above the edge match correctly the experimental spectrum. Thus, both models are in semi-quantitative agreement with the experimental XANES spectra, confirming that $Au^{III}Cl_4^-$ and $Au^ICl_2^-$ are the dominant Au species in the investigated solution at 22 and 250 °C, respectively. The mismatches between calculated and experimental amplitudes of XANES features might be attributed to the presence of a weak hydration shell around Au complexes in solution that was not considered by the present modeling. Such hydration is expected to have no detectable effect on the EXAFS signal which is poorly sensitive to distant and loosely bound shells, but it may influence the XANES spectra owing to their greater sensitivity than EXAFS to the atomic arrangement and cluster geometry. For example, solvation effects may slightly affect the amplitudes of the main XANES features as shown for the similar $CuCl_2^-$ species having a linear Cl–Cu–Cl geometry (Brügger et al., 2007). Work is currently in progress to explicitly account for the solvation effects on XANES spectra of Au complexes.

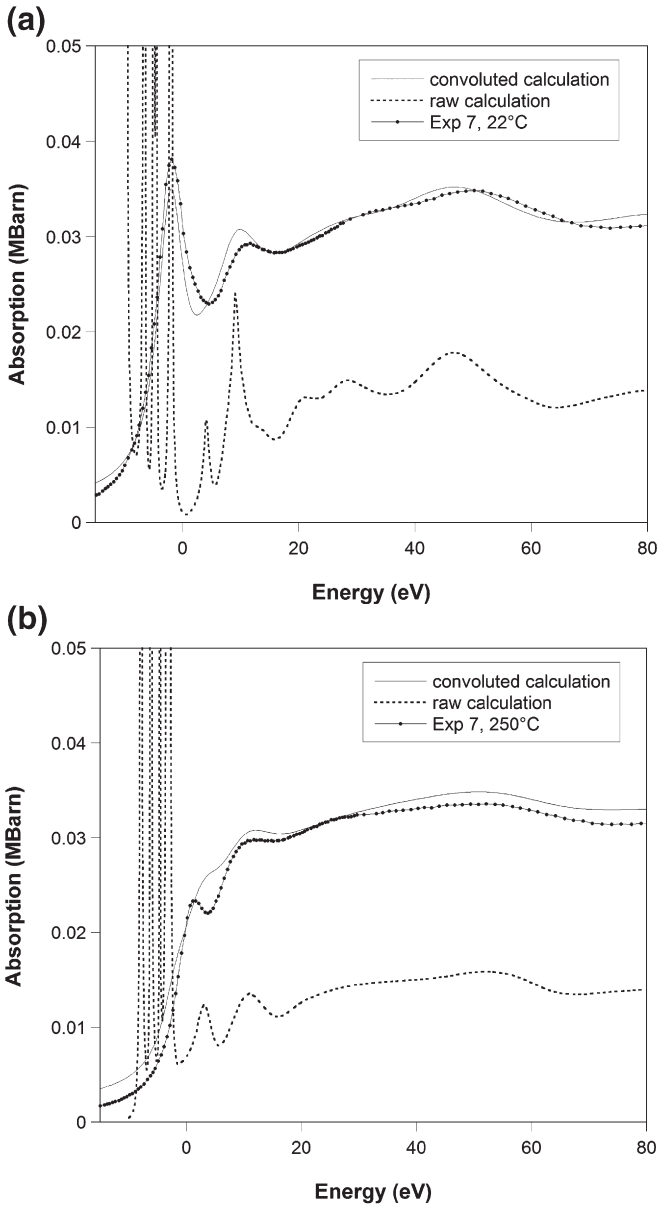

Fig. 8. XANES spectra of (a) $AuCl_4^-$ and (b) $AuCl_2^-$ aqueous species modeled using the FDMNES ab-initio code, and their comparison with experimental data (Exp 7 at 22 and 250 °C, 600 bar). The raw calculated spectra are scaled by ×0.4 for clarity. The energy of 0 eV on the X-axis corresponds to the L_{III} absorption edge of metallic Au at 11919 eV. The high-intensity 'spikes' below 0 eV in the raw spectra correspond to predicted electronic transitions that are not resolved in the convoluted spectra, which take into account the core-hole width and experimental resolution (see Section 2.4).

4. Discussion

4.1. Au^{III}–Au^I relationships and comparison with available Raman spectroscopy studies

The whole set of XANES and EXAFS results obtained in this study together with available thermodynamic data indicates that $AuCl_4^-$ and $AuCl_2^-$ are by far the dominant Au species in the investigated acidic Cl-bearing systems at $T \leq 100$ °C and $T \geq 250$ °C, respectively. In the intermediate T-range, in the $HAuCl_4$–NaCl–HCl system with and without $Au_{(s)}$, the fraction of each species can be thus quantified from XANES linear combination analyses (LCA) using, as the references, the XANES spectra of $AuCl_4^-$ and $AuCl_2^-$ obtained at 22 and 250 °C, respectively (Exp 7). The fraction of Au present as $AuCl_2^-$ ($Au_{tot} = AuCl_4^- + AuCl_2^-$) derived from the analysis of XANES spectra is reported in Table 1. Note that because of contrasting spectral shapes for Au^{III} and Au^I species, the limit of detection of each species fraction is very low, <3% of total Au, with a typical uncertainly less than 5%. This detection limit is much lower than that derived from the average number of chlorine atoms determined from EXAFS spectra (~10–20%) because of the much greater sensitivity of XANES than EXAFS to Au redox state and species geometry (linear Au^ICl_2 versus plane-square $Au^{III}Cl_4^-$) despite the similarities in Au–Cl bond lengths in both complexes (~2.27–2.28 Å). The accurate match of the experimental XANES spectra with the sum of the two end member species strongly suggests that no other complexes with different XANES signatures (e.g., $AuCl_3^{2-}$, $AuOH^0$) may be present in significant amounts. Thus, both EXAFS and XANES yield identical $AuCl_2^-/AuCl_4^-$ fractions within errors confirming again that these two species are largely dominant in our experimental systems.

It can be seen in Table 1 that in the $HAuCl_4$–NaCl–HCl solutions without gold, the reduction with increasing temperature of Au^{III} to Au^I is much slower in the (more inert) sapphire cell than in the carbon cell (Exp 2 versus Exp 3), but in both cases the precipitation of metallic Au, which starts at 250 and 150 °C, respectively, is always accompanied by the progressive formation of $AuCl_2^-$ at the expense of $AuCl_4^-$. These findings agree with the Raman spectroscopic study of Pan and Wood (1991) carried out on concentrated hydrochloric acid solutions (m_{HCl}=2–5) at P_{sat} using a Pyrex cell, which indicated the appearance of a new band at ~332 cm^{-1} above 100 °C, tentatively attributed to the $AuCl_2^-$ species. This assignment was, however, disputed in the more recent Raman spectroscopic study of Murphy et al. (2000) carried out on less acidic solutions similar to those of our study at comparable T–P conditions and using silica or glass pressure cells. These authors observed rapid Au precipitation at elevated temperatures from $HAuCl_4$–HCl solutions similar to our findings, but did not detect any new bands that might correspond to the $AuCl_2^-$ species, in contrast

with our XAFS evidence for $AuCl_4^-$ reduction to $AuCl_2^-$. This apparent disagreement might be related to the much lower sensitivity of Raman spectroscopy, in comparison to XAFS, to distinguish between the overlapping Au^{III}–Cl and Au^{I}–Cl vibrations which are expected to be very close following their almost identical bond lengths (within 0.01 Å) as found in our study (e.g., Raman frequencies for the stretching Au–Cl vibrations at ambient conditions are 324 and 329 cm^{-1}, respectively for $AuCl_4$ and $AuCl_2$ moieties in solid compounds, Braunstein and Clark, 1973; Murphy et al., 2000). Another possibility might be differences in cell-material properties between our and their study resulting in different redox potentials which might favor $AuCl_2^-$ stability in our experiments. A third possibility might be X-ray beam induced reduction, but no convincing demonstration of X-ray beam effects could be done in our study at least within the limited period of beam exposure (up to few hours).

In the presence of an excess of metallic gold in $HAuCl_4$–NaCl–HCl solutions, the fraction of $AuCl_2^-$ in solution increases with the temperature rise and is comparable in both the carbon and sapphire cells (Exp 4 versus Exp 1) at $T \leq 150$ °C, and it is also close to that measured in the absence of gold. At $T > 150$ °C, almost all Au is lost from solution in the carbon cell, but in the sapphire cell, $AuCl_4^-$ reduction to $AuCl_2^-$ increases and is accompanied by Au dissolution between 150 and 200 °C, followed by Au precipitation at $T \geq 250$ °C (Table 1, Figs. 2 and 3). These observations are in agreement with the Raman study of Murphy et al. (2000) which showed, on the basis of peak fitting procedures, a growth at $T \geq 250$ °C of the band at ~326 cm^{-1} tentatively attributed to the $AuCl_2^-$ species. Note, however, that quantification of species distribution and total dissolved Au concentrations was not possible from Raman spectra in contrast with XAFS spectra obtained in this study.

4.2. Comparison with thermodynamic calculations

The Au aqueous concentrations and species distribution obtained from XAFS spectroscopy can be compared with available thermodynamic data for aqueous Au species which are largely based on solubility measurements performed over a wide range of *T*–*P* and solution compositions. Detailed discussion of the different data sources, derivation of thermodynamic properties for some Au aqueous species, and computational details are reported in the Appendix, whereas calculated Au total concentrations and fractions of the major species in the solutions investigated by XAFS are listed in the Supplementary Table.

4.2.1. Metal-free $HAuCl_4$–NaCl–HCl system

In the metal-free $HAuCl_4$–NaCl–HCl solutions, calculations predict that $AuCl_4^-$ is the dominant species (>90%) and that no Au precipitation occurs to at least 300 °C. In contrast, our experiments show that at least 50% of total dissolved Au is reduced to $AuCl_2^-$ at $T < 250$ °C, and the major part of Au is precipitated above 250 °C both in carbon and sapphire cells. If this discrepancy may be easily explained for experiments in the carbon cell whose minor dissolution at elevated temperatures creates reducing conditions favorable for Au^{III} reduction as shown by thermodynamic calculations, the cause for Au reduction/precipitation phenomena observed in the inert sapphire cell remains unclear. It might result from beam-induced effects, as was observed for sulfite (SO_3) and thiosulfate (S_2O_3) aqueous solutions of monovalent gold at ambient temperature (Pokrovski, personal communication), and NaCl–NaOH solutions of trivalent gold at neutral-to-basic pH (Berrodier et al., 2004; Wang et al., 2007). Such effects were not observed, however, in the acidic Au^{III}–Cl solutions at ambient temperature over at least 2–3 h of beam exposure in this study, where Au^{III} is in the form of the extremely stable $AuCl_4^-$ complex. Similarly, no beam-induced Au precipitation was detected in XAFS experiments with the identical cell configuration in the system Au–S–NaOH where Au^{I} forms very stable hydrosulfide species (Pokrovski et al., 2006b). Thus, no convincing evidence for beam-induced effects in the Au^{I}–Cl system can be provided in this study likely owing to a combination of other factors (e.g., cell material, gas exchange etc.) which further complicate the spectroscopic investigation of certain redox-sensitive systems. Further systematic studies are necessary to quantitatively address the X-ray beam effects.

Note that the partial dissolution of He in the fluid at temperatures below 300 °C is too low to significantly affect water activity and thus decrease metal solubilities (see Section 2.1 for details). Assuming, in the worst case, an equilibrium between the experimental solution and helium gas, He solubility in pure water at 600 bar He and 250 °C is <2 mol% and is even less in the presence of electrolytes (NaCl), thus suggesting that He dissolution is unlikely to explain the observed low solubility.

Another possible cause for the observed discrepancy might be the loss of oxygen through the Viton seal rings (e.g., the oxygen fugacity in $AuCl_4^-/AuCl_2^-$ solutions (Exp 2) in the absence of $Au_{(s)}$ at 200 and 300 °C is predicted to be as high as 0.5 and 1 bar, respectively). Note also that the formation of a thin water film between the seal rings and the cell/piston walls may favor the escape of dissolved gas. Oxygen loss, together with fast reduction kinetics of dissolved Au at elevated temperatures may lead to precipitation of small quantities of metallic Au at $T > 100$ °C followed by massive Au precipitation at $T \sim 300$ °C. This could explain why the $AuCl_4^-/AuCl_2^-$ ratio in Exp 2 (initially metal-free) was close to that determined in the presence of metallic Au (Exp 1).

4.2.2. $HAuCl_4$–NaCl–HCl system with native gold at weakly acidic pH

In the weakly acidic (0.01 m HCl) $HAuCl_4$–NaCl–HCl system with an excess of Au metal examined in our study (Exp 1 and 4), thermodynamic calculations predict the formation of the $AuCl_2^-$, $AuOH^0$ and $AuCl^0$ aurous species at the expense of $AuCl_4^-$, and an increase of dissolved Au concentrations from ~0.04 to 0.10 m as temperature is raised from 100 to 300 °C (Supplementary Table). The predicted aqueous distribution of all Au–Cl species is in qualitative agreement with our XAFS findings, as well as the small amount of $AuOH^0$ calculated using gold solubility data from Zotov et al. (1985) and Vlassopoulos and Wood (1990) (see Appendix). Data of Stefánsson and Seward (2003a) yield somewhat higher concentrations of $AuOH^0$ at 100–300 °C (up to 45% of total aqueous Au) in contradiction with our XAFS spectra, which do not show the presence of oxygen atoms in the first coordination sphere of Au (Table 2) within the detection limit of XAFS spectroscopy ($N_O < \sim 0.1$–0.2 atoms).

Like in the metal-free system, XAFS-measured total Au concentrations at $T \geq 150$ °C are 1–2 orders of magnitude lower than those deduced from thermodynamic calculations. The reasons for that may be i) influence of the cell material (carbon in Exp 4), ii) beam-induced effects, and iii) equilibration of oxygen/hydrogen pressure with the external autoclave volume through the seal rings. Indeed, if the ratio of $AuCl_4^-/AuCl_2^-$ concentrations is independent of redox conditions (Eq. (2)), dissolved Au concentration is controlled by the oxygen (or hydrogen) contents according to the reactions

$$Au_{(s)} + 2Cl^- + H^+ + 0.25O_2 = AuCl_2^- + 0.5H_2O \quad (3)$$

$$Au_{(s)} + 4Cl^- + 3H^+ + 0.75O_2 = AuCl_4^- + 1.5H_2O \quad (4)$$

Thus, the loss of dissolved oxygen from the spectroscopic cell would result both in reduction of Au^{III} and in $Au_{(s)}$ precipitation. Quantification of the contributions of different factors affecting Au behavior in Cl-bearing systems at elevated temperatures will await further studies.

4.2.3. $HAuCl_4$–NaCl–HCl system with native gold at strongly acidic pH

In the more acidic and Cl-rich $HAuCl_4$–NaCl–HCl system (~0.5 m HCl–0.5 m NaCl) with an excess of native gold at 250 °C and 600 bar (Exp 7 in sapphire cell), calculations predict that more than 85% of

total Au is in the form of $AuCl_2^-$, with minor contributions from $AuCl^0$ (<10%) and $AuCl_4^-$ (<5%). This is in quantitative agreement with our EXAFS and XANES results which indicate that $AuCl_2^-$ accounts for more that 90% of total Au, with a possible presence of less than 5-10% of $AuCl^0$ or other species ($AuOH^0$), which is at the limit of spectral resolution. XAFS-derived aqueous Au concentrations are, however, at least an order of magnitude lower than the predicted values (0.05–0.10 m), and show a progressive decrease with time even after 2 h of measurement. Again, we are not able to account for these discrepancies. Considering the inert and tight nature of the Al_2O_3 cell used in this run, the most probable explanation would be Au reduction under the effect of X-ray irradiation which may cause water radiolysis and production of hydrogen radicals and solvated electrons (H^*, e^-) in solution that might be efficient reductants of Au^I species (e.g., Wang et al., 2007). More experiments are needed to quantitatively address this issue.

5. Concluding remarks

To our knowledge, this study provides the first measurements using in situ XAFS spectroscopy of the stability and structure of Au^{III} and Au^I chloride complexes at elevated temperatures and pressures pertinent to natural hydrothermal conditions. It demonstrates that XAFS spectroscopy can be used for direct measurement of both concentrations and the local atomic structures of metals in the complex and rapidly evolving fluid systems ubiquitous in high *T–P* geological environments.

Combination of classical XAFS spectral analysis with ab-initio quantum-chemical calculations of optimized geometries and XANES spectra of Au aqueous complexes allows accurate characterization of the identities and structures of the Au species responsible for the gold transport by high-temperature hydrothermal fluids. Our data provide direct spectroscopic evidence for the formation of the $AuCl_2^-$ complex in acidic saline hydrothermal fluids. This complex is linear, with Au–Cl distances of 2.267±0.004 Å, in agreement with Au^I crystal chemistry. The structural parameters for this species, derived for the first time, will allow an improved interpretation of Raman spectroscopic data and predictions of solvation effects in high *T–P* fluids.

This study also shows that the properties of the spectroscopic cell material and X-ray beam-induced effects may exert strong influence on redox-sensitive aqueous systems like that investigated in this study. Explicit account of these effects is required to unambiguously interpret in situ spectroscopic data at elevated *T–P*.

Acknowledgements

This work was supported by CNRS grants from the French programs GDR Transmet and 3F (Failles, Fluides, Flux), and a Russian RFBR grant (n° 07-05-72553). We are grateful to the ESRF and French CRG committees for providing beam time and access to the synchrotron facility. We are indebted to Olivier Geaymond and Eric Lahera for their help in the X-ray cell installation and running, and Rémi Bruyère and Alain Prat for the helium pressure regulation system. Bruce Ravel is thanked for his advice on the Athena and Artemis software, and Yves Joly for his assistance in XANES spectra modeling. François Farges is thanked for the helpful discussions on Au XAFS, and Joel Brugger, Cristian Doonan and Frank Reith are acknowledged for supplying $AuCl_{(s)}$ XANES spectra. We greatly appreciate the constructive remarks of the reviewer Terry Seward and an anonymous referee. We are grateful to the invited editor Andrew Berry for his very careful handling of this manuscript and pertinent comments and suggestions that significantly improved both the Science and English of this paper.

Appendix A. Supplementary data

Supplementary data associated with this article can be found, in the online version, at doi:10.1016/j.chemgeo.2008.09.007.

References

Akinfiev, N.N., Zotov, A.V., 2001. Thermodynamic description of chloride, hydrosulphide, and hydroxo complexes of Ag(I), Cu(I), and Au(I) at temperatures of 25–500 °C and pressures of 1–2000 bar. Geochem. Int. 39 (10), 990–1006.

Anderko, A., Pitzer, K.S., 1993. Equation-of-state representation of phase equilibria and volumetric properties of the system NaCl–H_2O above 573 K. Geochim. Cosmochim. Acta 57, 1657–1680.

Bakker, R.J., 2003. Package FLUIDS 1. Computer programs for analysis of fluid inclusion data and for modelling bulk fluid properties. Chem. Geol. 194, 3–23.

Becke, A.D., 1993. Density-functional thermochemistry. III. The role of exact exchange. J. Chem. Phys. 98, 5648–5652.

Benfield, R.E., Filipponi, A., Bowron, D.T., Newport, R.J., Gurman, S.J., 1994. An X-ray absorption study of gold coordination compounds: EXAFS refinements and double-electron excitation background. J. Phys., Condens. Matter 6, 8449–8468.

Berrodier, I., Farges, F., Benedetti, M., Winterer, M., Brown Jr., G.E., Deveughèle, M., 2004. Adsorption mechanisms of trivalent gold on iron- and aluminum-(oxy)hydroxides. Part 1: X-ray absorption and Raman scattering spectroscopic studies of Au(III) adsorbed on ferrihydrite, goethite, and boehmite. Geochim. Cosmochim. Acta 68, 3019–3042.

Braunstein, P., Clark, R.J.H., 1973. The preparation, properties and vibrational spectra of complexes containing the $AuCl_2^-$, $AuBr_2^-$ and AuI_2^- ions. J. Chem. Soc. Dalton Trans. 1845–1848.

Brugger, J., Etschmann, B., Liu, W., Testemale, D., Hazemann, J.-L., Emerich, H., van Beek, W., Proux, O., Tran, C., 2007. An XAS study of the structure and thermodynamics of Cu(I) chloride complexes in brines up to high temperature (400 °C, 600 bars). Geochim. Cosmochim. Acta 71, 4920–4941.

Crozier, E.D., Rehr, J.J., Ingalls, R., 1988. Amorphous and liquid systems. In: Koningsberger, D.C., Prins, R. (Eds.), X-ray Absorption: Principles, Applications, Techniques of EXAFS, SEXAFS and XANES. Wiley-Interscience, New York, pp. 373–442.

Cromer, D.T., Liberman, D., 1970. Relativistic calculations of anomalous scattering factors for X-rays. J. Chem. Phys. 53, 1891–1898.

Elam, W.T., Ravel, B.D., Sieber, J.R., 2002. A new atomic database for X-ray spectroscopic calculations. Radiat. Phys. Chem. 63, 121–128.

Farges, F., Sharps, J.A., Brown Jr., G.E., 1993. Local environment around gold(III) in aqueous chloride solutions: An EXAFS spectroscopy study. Geochim. Cosmochim. Acta 57, 1243–1252.

Feller, D., Glendening, E.D., Jong, W.A., 1999. Structures and binding enthalpies of $M^+(H_2O)_n$ clusters, M=Cu, Ag, Au. J. Chem. Phys. 110, 1475–1491.

Frisch, M.J., Trucks, G.W., Schlegel, H.B., Scuseria, G.E., Robb, M.A., Cheeseman, J.R., Montgomery Jr., J.A., Vreven, T., Kudin, K.N., Burant, J.C., Millam, J.M., Iyengar, S.S., Tomasi, J., Barone, V., Mennucci, B., Cossi, M., Scalmani, G., Rega, N., Petersson, G.A., Nakatsuji, H., Hada, M., Ehara, M., Toyota, K., Fukuda, R., Hasegawa, J., Ishida, M., Nakajima, T., Honda, Y., Kitao, O., Nakai, H., Klene, M., Li, X., Knox, J.E., Hratchian, H.P., Cross, J.B., Bakken, V., Adamo, C., Jaramillo, J., Gomperts, R., Stratmann, R.E., Yazyev, O., Austin, A.J., Cammi, R., Pomelli, C., Ochterski, J.W., Ayala, P.Y., Morokuma, K., Voth, G.A., Salvador, P., Dannenberg, J.J., Zakrzewski, V.G., Dapprich, S., Daniels, A.D., Strain, M.C., Farkas, O., Malick, D.K., Rabuck, A.D., Raghavachari, K., Foresman, J.B., Ortiz, J.V., Cui, Q., Baboul, A.G., Clifford, S., Cioslowski, J., Stefanov, B.B., Liu, G., Liashenko, A., Piskorz, P., Komaromi, I., Martin, R.L., Fox, D.J., Keith, T., Al-Laham, M.A., Peng, C.Y., Nanayakkara, A., Challacombe, M., Gill, P.M.W., Johnson, B., Chen, W., Wong, M.W., Gonzalez, C., Pople, J.A., 2004. Gaussian 03, Revision C.02. Gaussian, Inc., Wallingford CT.

Gammons, C.H., Williams-Jones, A.E., 1995. The solubility of Au–Ag alloy + AgCl in HCl/NaCl solutions at 300 °C: new data on the stability of Au(I) chloride complexes in hydrothermal fluids. Geochim. Cosmochim. Acta 59, 3453–3468.

Gammons, C.H., Williams-Jones, A.E., 1997. The disproportionation of gold(I) chloride complexes at 25 to 200 °C. Geochim. Cosmochim. Acta 61, 1971–1983.

Hay, P.J., Wadt, R.R., 1985. Ab initio effective core potentials for molecular calculations. Potentials for K to Au including the outermost core orbitals. J. Chem. Phys. 82, 299–310.

Henley, R.W., 1973. Solubility of gold in hydrothermal chlorine solution. Chem. Geol. 11, 73–87.

Joly, Y., 2001. X-ray absorption near-edge structure calculations beyond the muffin tin approximation. Phys. Rev. B 63, 125120.

Jones, P.G., Hohbein, R., Schwarzmann, E., 1988. Anhydrous sodium tetrachloroaurate (III). Acta Crystallogr. C 44, 1164–1166.

Kimball, G.E., Shortley, G.H., 1934. The numerical solution of Schrödinger's equation. Phys. Rev. 45, 815–820.

Lee, C., Yang, W., Parr, R.G., 1988. Development of the Colle–Slavetti correlation-energy formula into a functional of the electron density. Phys. Rev. B 37, 785–789.

Maeda, M., Ohtaki, H., Johansson, G., 1974. An X-ray investigation of the structures of the tetrachloro- and tetrabromoaurate(III) ions in aqueous solution. Bull. Chem. Soc. Japan 47 (9), 2229–2237.

Murphy, P.J., LaGrange, M.S., 1998. Raman spectroscopy of Au chloro-hydroxy speciation in fluids at ambient T and P: a re-evaluation of the effects of pH and chloride concentration. Geochim. Cosmochim. Acta 62, 3515–3526.

Murphy, P.J., Stevens, G., LaGrange, M.S., 2000. The effects of temperature and pressure on gold-chloride speciation in hydrothermal fluids: a Raman spectroscopic study. Geochim. Cosmochim. Acta 64, 479–494.

Newville, M., 2001. IFEFFIT: interactive XAFS analysis and FEFF fitting. J. Synchrotron Radiat. 8, 322–324.

Nikolaeva, N.M., Erenburg, A.M., Antipina, V.A., 1972. About the temperature dependence of the standard potentials of halogenide complexes of gold. Izv. Sibirskogo Otdeleniya AN SSSR, No. 9. Ser. Khim. Nauk, Vip., vol. 4, pp. 126–128 (in Russian).

Pan, P., Wood, S.A., 1991. Gold-chloride complexes in very acidic aqueous solutions and at temperatures 25–300 °C: a laser Raman spectroscopic study. Geochim. Cosmochim. Acta 55, 2365–2371.

Peck, J.A., Tait, C.D., Swanson, B.I., Brown Jr., G.E., 1991. Speciation of aqueous gold(III) chloride from ultraviolet/visible absorption and Raman/resonance Raman spectroscopies. Geochim. Cosmochim. Acta 55, 671–676.

Pokrovski, G.S., Bény, J.-M., Zotov, A.V., 1999. Solubility and Raman spectroscopic study of As(III) speciation in organic compound-water solutions. A hydration approach for aqueous arsenic in complex solutions. J. Solution Chem. 28, 1307–1327.

Pokrovski, G.S., Zakirov, I.V., Roux, J., Testemale, D., Hazemann, J.-L., Bychkov, A.Y., Golikova, G.V., 2002. Experimental study of arsenic speciation in vapor phase to 500 °C: implications for As transport and fractionation in low-density crustal fluids and volcanic gases. Geochim. Cosmochim. Acta 66, 3453–3480.

Pokrovski, G.S., Roux, J., Hazemann, J.-L., Testemale, D., 2005a. An X-ray Absorption spectroscopy study of argutite solubility and germanium aqueous speciation in hydrothermal fluids to 500 °C and 400 bar. Chem. Geol. 217, 127–145.

Pokrovski, G.S., Roux, J., Harrichoury, J.-C., 2005b. Fluid density control on vapor–liquid partitioning of metals in hydrothermal systems. Geology 33, 657–660.

Pokrovski, G.S., Borisova, A.Yu., Roux, J., Hazemann, J.-L., Petdang, A., Tella, M., Testemale, D., 2006a. Antimony speciation in saline hydrothermal fluids: a combined X-ray absorption fine structure and solubility study. Geochim. Cosmochim. Acta 70, 4196–4214.

Pokrovski, G.S., Tagirov, B.R., Schott, J., Hazemann, J.-L., Harrichoury, J-C., Roux, J., 2006b. Speciation of gold and associated metals at hydrothermal conditions: in situ experimental approaches and physical–chemical modeling. Actes du Colloque GDR Transmet — Bilan & Perspectives, Nancy 6–7 juillet 2006, pp. 91–94.

Pokrovski, G.S., Borisova, A.Yu., Harrichoury, J.-C., 2008a. The effect of sulfur on vapor–liquid fractionation of metals in hydrothermal systems. Earth Planet. Sci. Lett. 266, 345–362.

Pokrovski, G.S., Roux, J., Hazemann, J.-L., Borisova, A.Yu., Gonchar, A.A., Lemeshko, M.P., 2008b. In situ X-ray absorption spectroscopy measurement of vapour-brine fractionation of antimony at hydrothermal conditions. Min. Mag. 72 (2), 667–681.

Proux, O., Nassif, V., Prat, A., Ulrich, O., Lahera, E., Biquard, X., Menthonnex, J.-J., Hazemann, J.-L., 2006. Feedback system of a liquid-nitrogen-cooled double-crystal monochromator: design and performances. J. Synchrotron Radiat. 13, 59–68.

Proux, O., Biquard, X., Lahera, E., Menthonnex, J.-J., Prat, A., Ulrich, O., Soldo, Y., Trevisson, P., Kapoujyan, G., Perroux, G., Taunier, P., Grand, D., Jeantet, P., Deleglise, M., Roux, J.-P., Hazemann, J.-L., 2005. FAME: a new beamline for X-ray absorption investigations of very diluted systems of environmental, material and biological interests. Phys. Scripta T115, 970–973.

Ravel, B., Newville, M., 2005. ATHENA, ARTEMIS, HEPHAESTUS: data analysis for X-ray absorption spectroscopy using IFEFFIT. J. Synchrotron Radiat. 12, 537–541.

Rehr, J.J., 2006. Theory and calculations of X-ray spectra: XAS, XES, XRS, and NRIXS. Radiat. Phys. Chem. 75, 1547–1558.

Rehr, J.J., Albers, R.C., Zabinsky, S.I., 1992. High-order multiple-scattering calculations of X-ray-absorption fine structure. Phys. Rev. Lett. 69, 3397–3400.

Schott, J., Pokrovski, G.S., Tagirov, B.R., Hazemann, J.-L., Proux, O., 2006. First in situ XAFS determination of gold solubility and speciation in sulfur-rich hydrothermal solutions. Geochim. Cosmochim. Acta 70 (18A), 13.

Schwerdtfeger, P., Dolg, M., Schwarz, W.H.E., Bowmaker, G.A., Boyd, P.D.W., 1989. Relativistic effects in gold chemistry. I. Diatomic gold compounds. J. Chem. Phys. 91, 1762–1774.

Seward, T.M., Driesner, T., 2004. Hydrothermal solution structure: experiments and computer simulations. In: Palmer, D.A., Fernandez-Prini, R., Harvey, A.H. (Eds.), Aqueous Systems at Elevated Temperatures and Pressures. Elsevier, pp. 149–182.

Schulte, M.D., Shock, E.L., Wood, R.H., 2001. The temperature dependence of the standard-state thermodynamic properties of aqueous nonelectrolytes. Geochim. Cosmochim. Acta 65, 3919–3930.

Sherman, D.M., 2001. Quantum chemistry and classical simulations of metal complexes in aqueous solutions. Rev. Min. Geochem. 42, 273–317.

Stefánsson, A., Seward, T.M., 2003a. The hydrolysis of gold(I) in aqueous solutions to 600 °C and 1500 bar. Geochim. Cosmochim. Acta 67, 1677–1688.

Stefánsson, A., Seward, T.M., 2003b. Stability of chloridogold(I) complexes in aqueous solutions from 300 to 600 °C and from 500 to 1800 bar. Geochim. Cosmochim. Acta 67, 4559–4576.

Stevens, W.J., Krauss, M., Basch, H., Jasien, P.G., 1992. Relativistic compact effective potentials and efficient, shared-exponent basis sets for the third-, fourth-, and fifth-row atoms. Can. J. Chem. 70, 612–630.

Straehle, J., Loercher, K.P., 1974. Die Kristalldaten der Goldhalogenide $AuBr_3$ und AuCl. Zeit. Naturfor. Teil B29, 266–267.

Tagirov, B.R., Salvi, S., Schott, J., Baranova, N.N., 2005. Experimental study of gold-hydrosulphide complexing in aqueous solutions at 350–500 °C, 500 and 1000 bars using mineral buffers. Geochim. Cosmochim. Acta 69, 2119–2132.

Tagirov, B.R., Baranova, N.N., Zotov, A.V., Schott, J., Bannykh, L.N., 2006. Experimental determination of the stabilities $Au_2S(cr)$ at 25 °C and $Au(HS)_2^-$ at 25–250 °C. Geochim. Cosmochim. Acta 70, 3689–3701.

Testemale, D., Hazemann, J.-L., Pokrovski, G.S., Joly, Y., Roux, J., Argoud, R., Geaymond, O., 2004. Structural and electronic evolution of As(III) atomic environment in hydrothermal solutions: an EXAFS and XANES investigation. J. Phys. Chem. 121, 8973–8982.

Testemale, D., Argoud, R., Geaymond, O., Hazemann, J.-L., 2005. High pressure/high temperature cell for x-ray absorption and scattering techniques. Rev. Sci. Instrum. 76, 043905–043909.

Théobald, F., Omrani, H., 1980. Structure du tetrachloroaurate(III) de potassium dehydrate. Acta Crystallogr. B36, 2932–2935.

Tossel, J.A., 1996. The speciation of gold in aqueous solution: A theoretical study. Geochim. Cosmochim. Acta 60, 17–29.

Vlassopoulos, D., Wood, S.A., 1990. Gold speciation in natural waters: I. Solubility and hydrolysis reactions of gold in aqueous solution. Geochim. Cosmochim. Acta 54, 3–12.

Wang, C.H., Chien, C.C., Yu, Y.L., Lee, C.J., Lee, C.F., Chen, C.H., Hwu, Y., Yang, C.S., Je, J.H., Margaritondo, G., 2007. Structural properties of 'naked' gold nanoparticles formed by synchrotron X-ray irradiation. J. Synchrotron Radiat. 14, 477–482.

Wood, S., Crerar, D.A., Borcsik, M.P., 1987. Solubility of the assemblage pyrite–pyrrhotite–magnetite–sphalerite–galena–gold–stibnite–bismuthinite–argentite–molybdenite in H_2O–NaCl–CO_2 solutions from 200 to 350 °C. Econ. Geol. 82, 1864–1887.

Zabinsky, S.I., Rehr, J.J., Ankudinov, A., Albers, R.S., Eller, M.J., 1995. Multiple scattering calculations of X-ray absorption spectra. Phys. Rev. B 52, 2995–3009.

Zotov, A.V., Baranova, N.N., 1989. Thermodynamic properties of the aurochloride solute complex $AuCl_2^-$ at temperatures of 350–500 °C and pressures of 500–1500 bars. Sci. Geol. Bull. 42, 335–342.

Zotov, N., Keppler, H., 2002. Silica speciation in aqueous fluids at high pressures and temperatures. Chem. Geol. 184, 71–82.

Zotov, A.V., Baranova, N.N., Dar, ' yna, T.G., Bannykh, L.N., Kolotov, V.P., 1985. The stability of $AuOH^0_{sol}$ in water at 300–500 °C and 500–1500 atm. Geochem. Int. 22 (5), 156–161.